On the shear thickening flow of dilute CTAT worm-like micellar solutions

E. R. Macías

Departamento de Ingeniería Química, CUCEI, Universidad de Guadalajara, Boulevard M. Garcia Barragán 1451, Guadalajara, Jalisco 44430, México

F. Bautista

Departamento de Física, CUCEI, Universidad de Guadalajara, Boulevard M. Garcia Barragán 1451, Guadalajara, Jalisco 44430, México

J. F. A. Soltero and J. E. Puig

Departamento de Ingeniería Química, CUCEI, Universidad de Guadalajara, Boulevard M. Garcia Barragán 1451, Guadalajara, Jal. 44430, México

P. Attané

Laboratoire de Rhélogie, Universite J. Fourier, INPG, CNRS (UMR 5520), Boîte Postale 53, 38041, Grenoble Cedex 9, France

O. Manero[a]

Instituto de Investigaciones en Materiales, Universidad Nacional Autónoma de México, Apartado Postal 70-360, México, DF, 04510, México

Synopsis

Dilute solutions of worm-like micelles exhibit shear thickening caused by microstructural changes under specific flow conditions. In this work, for the first time, shear thickening in parallel plate and Poiseuille flows is investigated using simultaneously particle image velocimetry (PIV) and rheometry. Four distinctive zones of flow behavior are identified in parallel plates as the shear rate increases, namely, a Newtonian region, a transition regime where inhomogeneous nucleation of the shear-induced structures (SIS) is followed by homogeneous nucleation of SIS, and an apparent second-Newtonian regime at high shear rates, where rapid temporal fluctuations of the viscosity are smoothed out by inertia of the moving plate. In pipe pressure flow, PIV results reveal a flow pattern consisting of a superposition of two parabolic regions of the velocity profile located near the center and close to the pipe walls, and a transition region where again strong fluctuations in the velocity profile are observed. The experimental results are compared with predictions of a convected Maxwell constitutive equation coupled to a kinetic equation that accounts for an increase in dissipation of the system due to the presence of the SIS. The model accounts for the average steady values of the viscosity in the structured thickened state. © *2003 The Society of Rheology.* [DOI: 10.1122/1.1562479]

---

[a]Author to whom correspondence should be addressed; electronic mail: manero@servidor.unam.mx

I. INTRODUCTION

Dilute solutions of worm-like micelles often exhibit shear thickening flow, i.e., an increase in shear viscosity upon an increase in shear rate. Since the first reports on this phenomenon [Gravsholt (1980); Rehage and Hoffmann (1982)], shear thickening behavior has received ample attention [Rehage et al. (1986); Wunderlich et al. (1987); Kalus et al. (1989); Hoffmann et al. (1991); Hu et al. (1993, 1998a, 1998b); Hu and Mattys (1995); Liu and Pine (1996); Prötzl and Springer (1997); Berret et al. (1998)]. There is general agreement that shear thickening is caused by the formation of shear-induced structures (SIS), which have been recently detected by small-angle neutron scattering (SANS) [Berret et al. (1998)] and visualised by flow-light scattering [Hu et al. (1998a)].

It is known that shear thickening manifests itself in surfactant solutions at concentrations where there are locally elongated micelles. SIS develop at a critical shear rate ($\dot{\gamma}_c$) that depends on the surfactant concentration and temperature [Hu et al. (1993); Hartmann and Cressely (1997, 1998); Berret et al. (1998); Gámez-Corrales et al. (1999)]. At this critical shear rate, the viscosity increases abruptly from values close to that of the solvent (water) to values 2–10 times larger. This increase in viscosity usually takes a very long time. This *induction time* depends on the concentration and geometry and may sometimes be on the order of minutes, i.e., tens to hundredths the characteristic times of the sample. In addition, the shear thickening state is characterized by time-dependent viscosity fluctuations, which are usually larger near the critical shear rate.

Microscopic theories and models to explain shear thickening in dilute surfactant solutions are scarce. Preliminary attempts to describe this phenomenon include theories that incorporate nonequilibrium shear-induced phase transitions and hydrodynamic instabilities [Rehage and Hoffmann (1982); Olmsted and Lu (1997); Porte et al. (1997)]. Recently, Goveas and Pine (1999) introduced a simple phenomenological model to describe shear thickening flow of surfactant solutions. In their model, they assumed that a reaction takes place in the solution and forms a gel-like phase, in which there is no flow. With these assumptions, they were able to predict a re-entrant region in the stress–shear rate curve, which can be determined under stress-controlled conditions, and discontinuity in the stress–shear rate curve under strain rate-controlled conditions.

Four regimes have been identified in steady shear experiments as the shear stress is increased in solutions that exhibit shear thickening behavior [Hu et al. (1998a)]. The first regime (I) is Newtonian and occurs at stresses or shear rates smaller than a critical value. In this regime, the viscosity of the system is not larger than a few solvent viscosities. The second regime (II) occurs over an intermediate range of stress where the steady state is attained only under stress-controlled conditions. The shear rate in regime II is nearly constant or slightly decreases (depending on the geometry used) as the stress is increased. In this regime, large fluctuations in the shear rate are observed that have been associated to inhomogeneous nucleation of the SIS. Sometimes multiple shear stress values have been observed for a given shear rate in Couette geometry [Liu and Pine (1996); Gámez-Corrales et al. (1999); Macías et al. (2001)]. A further increase in the stress produces increasing values of the shear rate but SIS are still formed by inhomogeneous nucleation. At higher shear stresses, SIS homogeneous nucleation takes over (regime III). In this regime, the shear rate increases with an increase in shear stress. Under conditions of strain rate control, the steady state behavior passes directly from regime I to regime III. At even higher stresses, a fourth regime is observed, in which fracture or mechanical breakdown of the SIS formed occurs. Data support the description of a nonequilibrium phase transition taking place between the first and third regimes. However, SANS mea-

surements suggest that micelles grow and become aligned under shear and yield SIS without forming another phase, i.e., no phase transition occurs [Berret *et al.* (2001)].

Experimental results on shear thickening solutions under pressure flow include investigations of practical problems such as drag reduction in turbulent flow. For this, inhomogeneities in the sheared fluid are important and the shear-induced structures formed under flow directly affect the velocity field. This is relevant even in laminar flow, for which there is little information about the effects of the SIS on the velocity field. Wunderlich and Brunn (1989) determined the velocity field for cetyltrimethylammonium salycilate and NaBr solutions in two-dimensional channel flow by laser-Doppler anemometry and found that the velocity fluctuations, which were attributed to turbulence, increase above a critical shear rate. But, it may be possible that the velocity fluctuations were produced by the fracture of the SIS and by elastic instabilities. The experimental technique used, however, did not allow online determination of the entire flow field. Experimental difficulties arise, of course, because of the nature of the analysis of the flow field, based upon mean temporal values when the SIS and the fluid phase coexist. In this respect, particle image velocimetry (PIV) has the advantage of determining instantaneous flow field [Macías *et al.* (2001)]. This technique has been used to reveal the presence of slip layers at the wall of a Couette cell [Hu *et al.* (1998a, 1998b); Koch *et al.* (1998); Macías *et al.* (2001)].

In this article, the pipe flow of dilute cetyltrimethylammonium tosilate (CTAT) micellar solutions that are known to exhibit shear thickening behavior [Gámez-Corrales *et al.* (1999)] is examined by PIV with the goal of determining the velocity profiles at shear rates within the four regions identified by Hu *et al.* (1998a) and obtaining additional information on SIS effects on Poiseuille flow. Moreover, the steady-state rheology of shear thickening of these dilute aqueous solutions is analyzed with a simple model that captures many of the features of the linear [Soltero *et al.* (1996); Manero *et al.* (2002)] and the nonlinear viscoelastic behavior of such systems in the semidilute and concentrated regimes [Soltero *et al.* (1999); Bautista *et al.* (2000)]. This model, composed of the upper convected Maxwell equation and a kinetic equation for breaking and reformation of the micelles, is able to describe the shear banding behavior in steady simple shear. The pressure-driven pipe flow of shear thinning CTAT–water solutions was also reproduced by an extended version of this model [Bautista *et al.* (2002)]. The predictions of the model without any fitting parameters are compared with our experimental results and with others reported in the literature for both simple-shear and pipe flows.

II. EXPERIMENT

CTAT (Sigma) had a purity of 98%. It was purified by dissolving it in chloroform and precipitating it with ethyl ether. Water was doubly distilled and de-ionized.

Dilute solutions of CTAT (0.07–2.0 wt %) were prepared by weighing the appropriate amounts of CTAT and water in glass vials. These vials were placed in a water bath at 60 °C for a week where they were frequently shaken. Then samples were allowed to reach equilibrium at the temperature of measurement. All samples were centrifuged to remove suspended air bubbles before being tested.

For PIV experiments, a small amount (0.03 wt %) of plated glass reflecting particles (average diameter of 15 μm) was added to each of these solutions. Then the micellar solutions containing the glass particles were placed in the container of the PIV apparatus (DANTEC), which has a measuring cell that enables the detection of the point velocities across a capillary tube. The test section is a glass tube with inner and outer diameters of 4 and 6 mm, respectively, and 300 mm length, providing a L/D ratio of up to 75. The
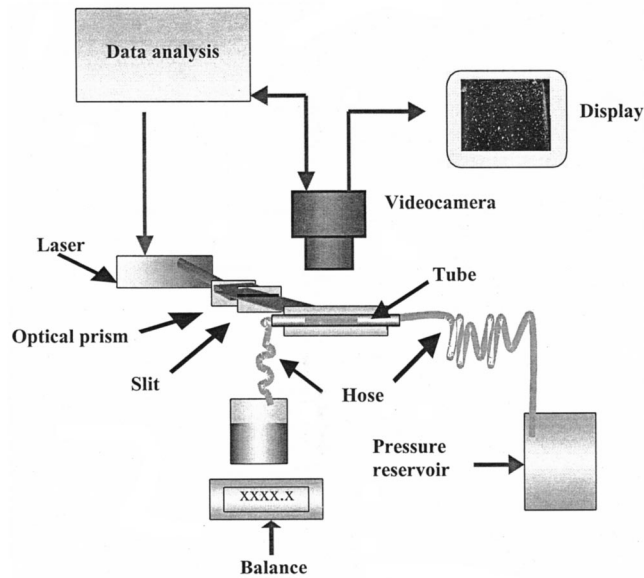
FIG. 1. Schematics of the PIV experimental setup for pipe flow.

measuring section was preceded by a plastic tube 6 mm in diameter and 8 m in length. The volumetric flow rate was controlled using the pressure exerted by compressed nitrogen. Flow rate measurements were made using a PIV-2000 computer-controlled balance. PIV measurements were carried out using a double-head YAG laser and a double-frame charge coupled device (CCD) camera with 768×484 pixel resolution, which is capable of taking pictures every 2 μs. The size of the light source was set at 100 μm width. The measuring section was kept inside a thermostat controlled bath at room temperature that was filled with the same test fluid to prevent optical distortion. The measuring section can provide velocity profiles at three different axial distances from the entrance (see Fig. 1). This arrangement enables one to observe the development of the velocity profile and to verify if the flow has reached steady-state conditions. Several flow conditions were tested, with shear rates in the range of 211–2067 s^{-1} that corresponds to overall Reynolds numbers from 423 to 4134. Before using the surfactant solutions, water was passed through the test section to visualize the velocity profile and to measure experimental errors attributed to deviations from the parabolic shape.

Steady simple shear data were measured in a Carri-Med CLS 500 stress-controlled rheometer equipped with a parallel plate cell with an optical plate of 6 mm and a gap of 2.286 mm (see Fig. 2). In addition, a cone and plate geometry with a diameter of 4 cm and an angle of 1.57° was used in some experiments.

III. MODEL

The model used here has been given attention elsewhere [Bautista *et al.* (1999)]. It consists of an upper convected Maxwell constitutive equation coupled to a kinetic equation that governs modification of the structure due to flow. For simple shear flow, the following ordinary differential equations apply:

$$\sigma + \frac{1}{G_0 \varphi} \frac{d\sigma}{dt} = \frac{\dot{\gamma}}{\varphi}, \tag{1}$$
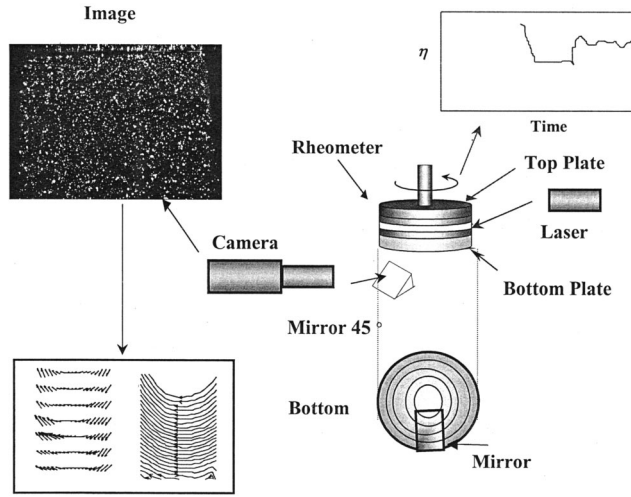
FIG. 2. Schematics of the PIV experimental setup for parallel plates.

$$\frac{d\varphi}{dt} = \frac{1}{\lambda}(\varphi_0 - \varphi) + k(\varphi_\infty - \varphi)\sigma\dot{\gamma}. \tag{2}$$

Here σ is the shear stress, $\dot{\gamma}$ is the shear rate, φ is the reciprocal of the shear viscosity (η^{-1}) or fluidity, with values of φ_0 and φ_∞ at zero- and infinite-shear rate, respectively; G_0 is the plateau modulus, λ is a structure relaxation time, and k is a kinetic constant for structure modification.

In steady shear flow, the shear component can be obtained by setting the time derivative to zero in Eqs. (1) and (2), leading to

$$\varphi^2 - \varphi_0\varphi - k\lambda(\varphi_\infty - \varphi)\dot{\gamma}^2 = 0. \tag{3}$$

The model contains five parameters to predict experimental data: φ_0, φ_∞, G_0, k, and λ, which can be estimated from independent rheological experiments, described elsewhere [Bautista *et al.* (2000)]. However, in steady simple shear, the model needs only three parameters, since the product $k\lambda$ appears in Eq. (3) as a single parameter. Notice also that the shear-induced structure is characterized by a modulus G_0 and a specific relaxation time. However, for steady-state predictions, the value of G_0 is not required.

In parallel plates, the tangential velocity and shear rates are given by

$$v_\theta(r) = \frac{\Omega r z}{h} = \dot{\gamma}(r)z, \tag{4}$$

where Ω is the angular velocity, z is the axial distance between the plates, r is the radial distance, h is the plate separation, and $\dot{\gamma}$ is the shear rate. The torque is given by

$$M(r) = 2\pi \int_0^{\dot{\gamma}_R} \left(\frac{R}{\dot{\gamma}_R}\right)^3 \dot{\gamma}^2 \sigma_{12} d\dot{\gamma}. \tag{5}$$

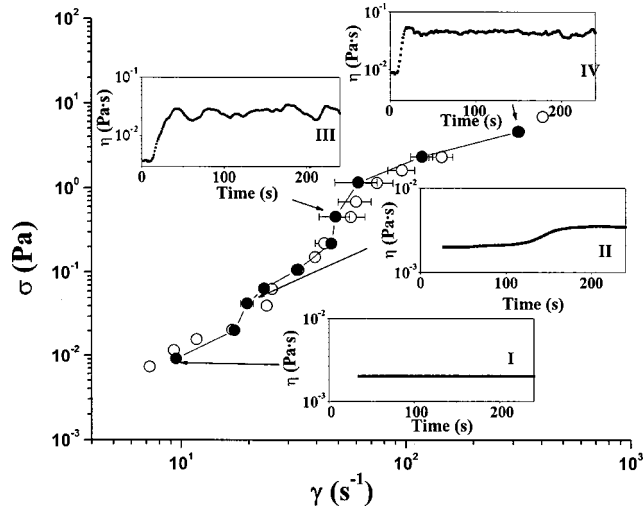Defining the apparent shear stress as

FIG. 3. Experimental shear stress vs the shear rate obtained in steady shear with parallel plates for 0.25 wt % CTAT solutions, depicting various regions of flow behavior: with (●) and without (○) reflecting glass particles. The variation of viscosity vs time corresponding to I, II, III, and IV regimes is shown in the insets.

$$\sigma_a = \dot{\gamma}(r)/\varphi(r) = \frac{2M(r)}{\pi R^3},\tag{6}$$

then, from Eq. (4)

$$v_\theta(z = h) = \frac{2hM(r)\varphi(r)}{\pi R^3}.\tag{7}$$

Equations (3)–(7) calculate the radial variation of the velocity given an applied shear stress. In Poiseuille flow, the velocity profile can be obtained from the following expression:

$$v_z = \frac{\Delta P}{2L}\int_r^R \varphi(r)rdr.\tag{8}$$

IV. RESULTS

A. Parallel plate experiments and steady simple shear flow predictions

Various regimes of flow behavior along the shear stress–shear rate curve measured in parallel plates are depicted in Fig. 3. In regime I the solution behaves as a Newtonian fluid. This region is reproducible in Couette measurements reported elsewhere [Macías *et al.* (2001)]. However, the occurrence and shape of the shear thickening curve in Couette and in parallel plates geometries are different. Shear thickening is observed in regimes II and III, especially in regime III where strong fluctuations in the viscosity indicate the appearance of homogeneous SIS nucleation. As pointed out elsewhere [Macías *et al.* (2001)], classical hydrodynamic behavior is observed in regime I, i.e., when SIS are not present. In regime II, a clearly defined steady state is obtained. Macías *et al.* (2001) reported that, during the induction period, the flow field is rheometric, i.e., there is a linear increase in the tangential velocity with the radius and no radial velocity component; however, after shear thickening, the velocity profiles are nearly linear and time
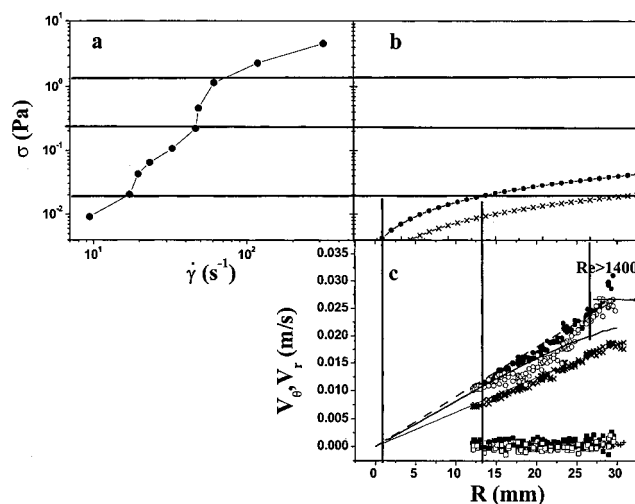
FIG. 4. (a) Experimental shear stress vs shear rate data obtained in steady shear with parallel plate geometry for 0.25 wt % CTAT solutions; (b) shear stress as a function of the radial position for several stress values at the rim of the plates; and (c) radial and tangential components of the velocity field as a function of the radial distance in regime II. The data were measured at 90 ($\bullet$) and 234 s ($\bigcirc$). The stress applied was 0.04 Pa. The crosses depict data of regime I. The dashed and solid lines in (c) represent the predicated tangential velocity profiles of the fluid before and after the thickening transition, respectively.

independent in the core of the flow, but deviate from linearity and vary over time at the rim of the plate. PIV indicates that the oscillations observed in regime III correspond to strong changes in the flow field. The radial velocity component is no longer negligible and the tangential velocity is strongly distorted from the linear profile over the whole domain in this regime. Fracture of the sample at the rim of the plate is suggested by the strong spatial variations. In regime IV, a nearly steady-state viscosity is observed. PIV data suggest rapid temporal fluctuations with fractured zones of solid-like displacements. These temporal variations are smoothed out by inertia of the moving plate, which may explain the appearance of steady state. Notice that the data obtained with (open circles in Fig. 3) and without (closed circles in Fig. 3) glass particles are very similar in the whole shear rate range examined. This means that the presence of the glass particles does not disturb the flow patterns, so the flow fields obtained (see Fig. 4) are representative of shear thickening flow and SIS formation.

The flow fields of a 0.25 wt % CTAT sample corresponding to regimes I and II are depicted in Fig. 4. Here, the stress at the rim of the plate versus the shear rate [Fig. 4(a)], the stress as a function of the radial position [Fig. 4(b)], and the tangential (v_θ) and radial (v_r) velocity components [Fig. 4(c)] obtained by PIV, are presented. Velocity components are obtained for radii larger than 13 mm in a horizontal rectangular experimental window (around 30 mm$\times$25 mm^2) located midway from the two planes. For stresses lower than 0.02 Pa, the flow is Newtonian (regime I) and the tangential component of the velocity [crosses in Fig. 4(c)] increases linearly with the radius whereas the radial component is zero, as expected. When the stress at the rim is increased to 0.04 Pa, which corresponds to region II [Fig. 4(a)], the induction time for this sample is 155 s. For times shorter than the induction time, v_θ deviates slightly from linearity [closed circles in Fig. 4(c)] whereas v_r deviates slightly from zero [Macías *et al.* (2001)]. However, for times longer than the induction time, the apparent viscosity increases 30% and deviations from linearity in v_θ are quite drastic [open circles in Fig. 4(c)]. In addition, the curve of stress
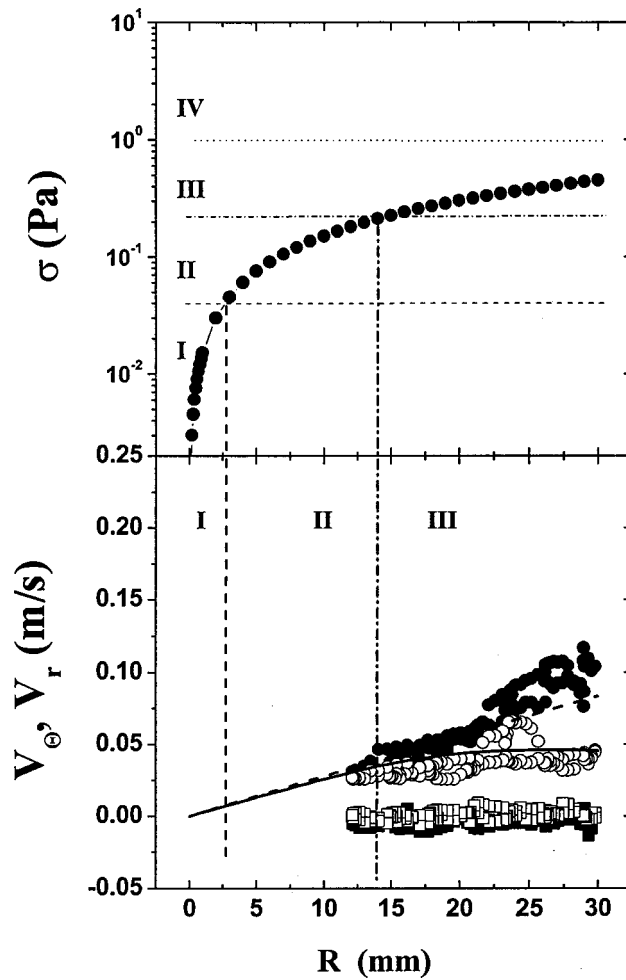
FIG. 5. (a) (Top) Shear stress as a function of the radial position for shear stress at the rim of the plate in regime III. (b) (Bottom) Tangential and radial components of the velocity field in regime III measured at 28 (●) and 35 s (○) of flow time. Model predictions for the low and high viscosity fluids are shown as dashed and solid lines, respectively.

versus radius indicates that for radius less than 13 mm, the stress curve is located in region I, while for radius larger than this value, the stress–shear rate curve is located in region II [Fig. 4(b)]. In Fig. 4(c), the line that separates region I from region II (located at 13 mm) represents the boundary between the low-viscosity Newtonian fluid and the high viscosity fluid when the stress is 0.04 Pa. The dashed and solid lines in Fig. 4(c) represent the predicted tangential velocity profiles of the fluid before and after the thickening transition, respectively. Model predictions simulate well the change in slope due to increased viscosity of the solution. Because for radius smaller than 13 mm the stress falls in region I, which is Newtonian, the tangential velocity should vary linearly. In fact, data below this boundary line fall onto the theoretical line. Unfortunately, our PIV apparatus does not allow taking data for radius smaller than, say, 11 mm to confirm this hypothesis. However, in the range from 11 to 13 mm the behavior is that of regime I. In addition, for

radial distances larger than 27 mm, the Reynolds number exceeds that of laminar flow, and the apparent rise in the tangential velocity is ascribed to the presence of a turbulent regime.

Figure 5 reports v_θ and v_r as a function of the radius for a 0.25 wt % CTAT sample, when the shear stress applied at the rim of the plate is in regime III [Fig. 5(a)]. In this situation, the fluid is subjected to stress within regions I, II, and III. The tangential velocity of the fluid in radial positions within region III deviates strongly from linearity and fluctuates spatially. We associate the velocity fluctuations with changes in time of the viscosity shown for region III in Fig. 3. The closed circles in Fig. 5 correspond to velocities displayed by the low-viscosity fluid (at 28 s of flow time), whereas the open circles in Fig. 5 correspond to velocities displayed by the high value of the fluctuating viscosity in Fig. 3 (at 35 s of flow time). Model predictions for the low and high viscosity fluids are shown as dashed and solid lines, respectively. As the radial distance increases, the shear stress and the tangential velocity increase up to the radial position where the shear stress exceeds the first critical value. In this regime, the velocity profile becomes nonlinear and attains almost constant values for larger radial distances, since the system shear thickens. The steady-state predictions of the high viscosity fluid are indicated in Fig. 5(b) by a solid line. Notice that the predictions again follow the viscosity changes of the system.

When the stress applied at the rim of the plate is in region IV (Fig. 6), the fluid is subjected to stress in the four regions. Here PIV data, collected in less than 1 s, exhibit strong fluctuations and solid-like displacements. Again, the PIV arrangement did not allow collecting data for radius smaller than around 11 mm and, therefore, the flow regimes that appear for radius smaller than this value could not be examined. Here, it was not possible to associate the amplitude of the fluctuations in viscosity (shown in Fig. 3, regime IV) with fluctuations in the velocity. In fact, the recorded fluctuations in the tangential velocity are much larger than those of the viscosity, as observed in Fig. 6(b). It is suggested that those rapid variations in less than 1 s are smoothed out by the inertia of the moving plate. Model predictions for the upper values of the fluctuating viscosity are shown in Fig. 6(b). Initially, for small radial distances the velocity increases linearly. As the radial distance increases the velocity profile becomes nonlinear and shows a maximum where regions of high velocity coexist with regions of low tangential velocity. In fact, the predictions of the thickened fluid show that the tangential velocity becomes multivalued as a function of the radial distance. The experimental results for radial distances larger than 13 mm show an almost linear profile in the low viscosity fluid that coexists with a high viscosity fluid with almost constant velocity.

Model predictions and experimental measurements in simple shear flow made in the cone and plate geometry for CTAT solutions at several concentrations (at 25 °C) are shown in Fig. 7. In Table I, the model parameters are given for each surfactant concentration at two temperatures. The solid lines represent the predictions of the model over a wide range of CTAT concentrations in both shear thickening and shear thinning regions. Notice that at 25 °C and CTAT concentrations of around 2 wt %, shear thinning behavior develops and a stress plateau appears over a range of shear rates, which suggests the existence of banded flow, as discussed by Bautista *et al.* (2000). For concentrations smaller than 2 wt %, the stress plateau fades and a monotonic increasing relationship between shear stress and shear rate is observed. From 2.0 down to 1.3 wt %, shear thinning is detected. Newtonian behavior is observed at 1.3 wt % CTAT. Between 1.3 and 0.8 wt %, incipient shear thickening flow appears (here the increase in viscosity is very small). At concentrations between 0.8 and 0.07 wt %, the shear thickening behavior is well defined. The increase in shear viscosity is around 50-fold. The shear rate range for
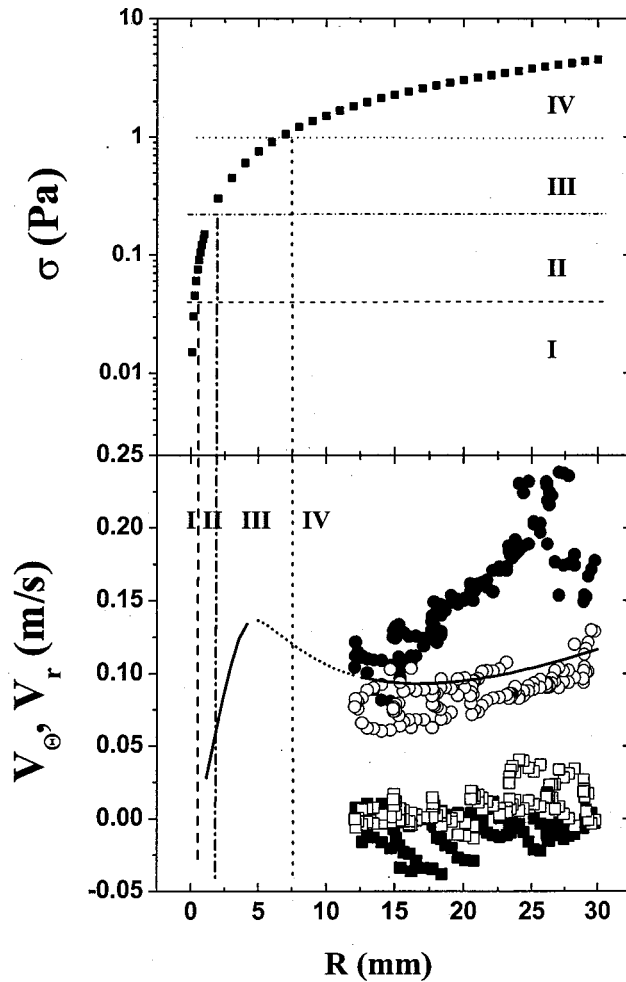
FIG. 6. (a) (Top) Shear stress as a function of the radial position for shear stress at the rim of the plate in regime IV. (b) (Bottom) Tangential and radial components of the velocity field in regime IV. Model predictions for the upper values of the fluctuating viscosity are shown.

shear thickening is from 30 to 100 s^{-1} for the 0.07 wt % sample and from 10 to 25 s^{-1} for the 0.8 wt % sample, the latter being steeper. For CTAT concentrations lower than 0.07 wt %, Newtonian behavior is again observed. On the other hand, the intensity of shear thickening diminishes with temperature (not shown). Also, the concentration at which shear thickening starts to be observed increases with the temperature and the range of shear rate for shear thickening shifts toward higher shear rates as the temperature is raised (not shown).

Figure 8 describes the concentration dependence of σ_c (lower critical stress) and σ_s (upper critical stress) at 25 °C. The latter is weakly dependent on the concentration, whereas the former varies strongly with the concentration for CTAT concentrations larger than 0.3 wt %. Discontinuity for both critical stresses occurs at around 0.8 or 0.9 wt %, indicating the transition to the shear thinning regime. Notice that the jump at discontinuity is more than a decade. Another transition, that between the dilute and semidilute regimes in the zero shear rate viscosity at 25 °C, has been reported at 0.5 wt % CTAT
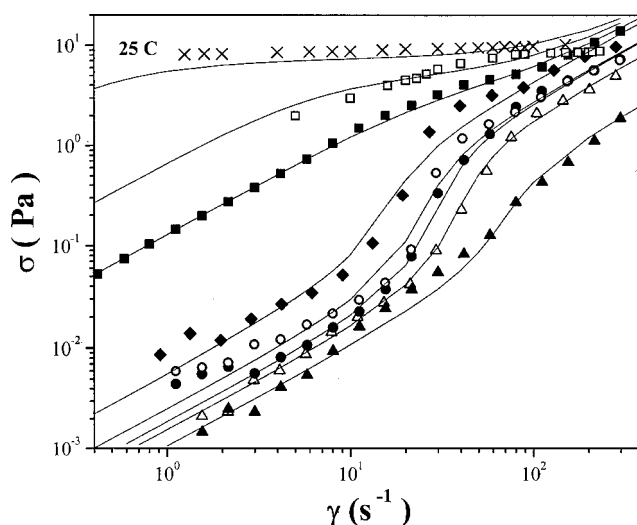
FIG. 7. Experimental and predicted shear stress vs the shear rate measured in cone and plate geometry at 25 °C for various concentrations: 0.07 (▲), 0.25 (△), 0.40 (●), 0.5 (○), 0.8 (◆), 1.0 (■), 1.5 (□), and 2.0 (×).

[Gámez-Corrales *et al.* (1999)]. This transition is also observed in Fig. 8 as the abrupt increase of the critical stress at 0.3 wt %.

The growth of viscosity as a function of time for stress-controlled experiments is shown in Fig. 9. In Fig. 9, shear stress is imposed and the growth of viscosity is measured as a function of time for stress levels within regimes I, II, III, and IV. It is necessary to remark that plate inertia leads to an apparent decrease in viscosity at the inception of shear, but does not modify the induction time. Corrections were made by subtracting data for water. According to available experimental results [Hu *et al.* (1998a)], the induction time is different and depends on whether shear stress or a shear rate is imposed.

In Fig. 10, the induction time versus stress applied is reported for the stress-controlled mode. In agreement with data reported by Hu *et al.* (1998a), the induction time measured here also depends on whether strain- or stress-controlled mode is used. As displayed, the

TABLE I. Model parameters used in the predictions shown in Fig. 7.

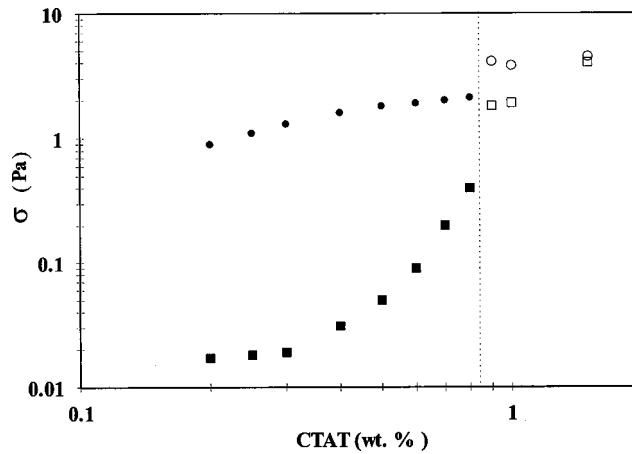| Concentration (wt %)	$T = 25\,°C$			$T = 30\,°C$		
	φ_0	φ_∞	$k\lambda$	φ_0	φ_∞	$k\lambda$
0.07	950	150	0.2	920	480	0.025
0.2	920	56	0.38	910	380	0.0195
0.25	650	50	0.45	660	210	0.025
0.3	640	48	0.51	600	200	0.05
0.4	530	36	0.64	520	155	0.05
0.5	400	35	0.68	350	137	0.058
0.6	240	26	0.68	260	107	0.06
0.7	180	23	0.71	175	105	0.063
0.8	160	21	0.77	140	105	0.063
1.0	7.8	20	0.03	42	107	0.0013
1.5	1.5	19.5	0.002			
2.0	0.08	19	0.001			
3.0	0.015	22	0.000 076			

FIG. 8. Concentration dependence of the critical shear stress, σ_c (squares) and σ_s (circles) at 25 °C. Closed symbols indicate the shear thickening regime and open symbols the transition one.

inverse proportionality between the induction time and applied stress holds in the low stress region around 0.05–0.7 Pa. Our model predicts also the inverse proportionality between the induction time and the applied stress or shear rate. However, the predicted induction times are 10–100 times faster. The reason for the discrepancy in the magnitude of the induction times lies in the fact that, in the experiments, inertia of the plates is mixed with the induction time, and since the model is not intended to predict plate inertia, then the predicted induction time is much shorter than the experimental one.

B. Poiseuille flow: Predictions and comparisons with experiments

The relationship between the steady simple shear curve [Fig. 11(a)], the stress as a function of the radial position [Fig. 11(b)], and the velocity profiles [Fig. 11(c)] in Poiseuille flow can be predicted with Eq. (8) of our model.
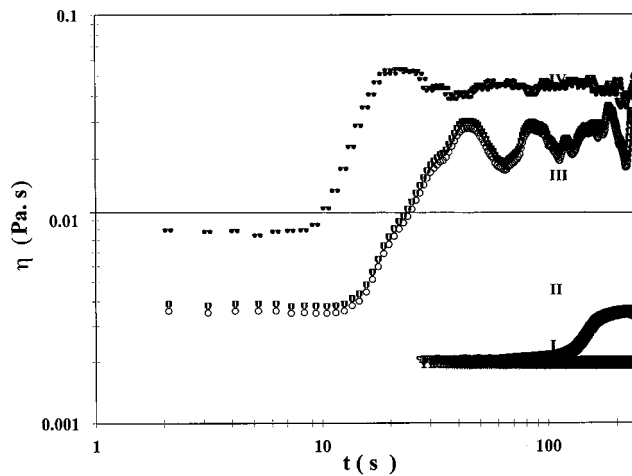

FIG. 9. Shear viscosity as a function of time in a stress-controlled experiment. The different experimental regimes (see the text) are indicated.
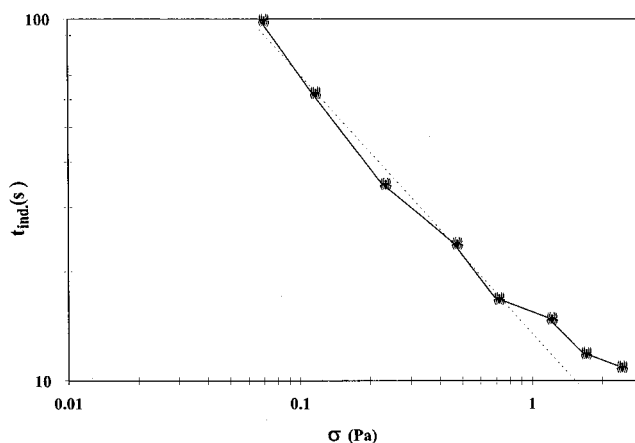
FIG. 10. Experimental data for the induction time as a function of the stress applied.

For shear stresses smaller than σ_c [curve A in Fig. 11(b)] or larger than σ_s [curve C in Fig. 11(b)], the parabolic profile of a Newtonian fluid in a pipe is predicted, except for a small region near the pipe center for curve C because of the radial dependence of the stress which causes induction of SIS [profile shown by thick lines in Fig. 11(c)]. When the shear stress [whose variation with the radius is indicated in the semilogarithmic plot of Fig. 11(b)] reaches values inside the region corresponding to those in regime II [curve B in Fig. 11(b)], the model predicts a transition region between two parabolas where a change of curvature in the velocity profile is observed. The shear rate in the vicinity of the wall is smaller than that resulting from extrapolation of the parabola positioned at the pipe center, indicating that a more viscous liquid layer flows close to the walls, corresponding to the shear-thickened regime III of high viscosity. This will geometrically determine the region in the pipe where shear thickening manifests itself. In addition, Fig.
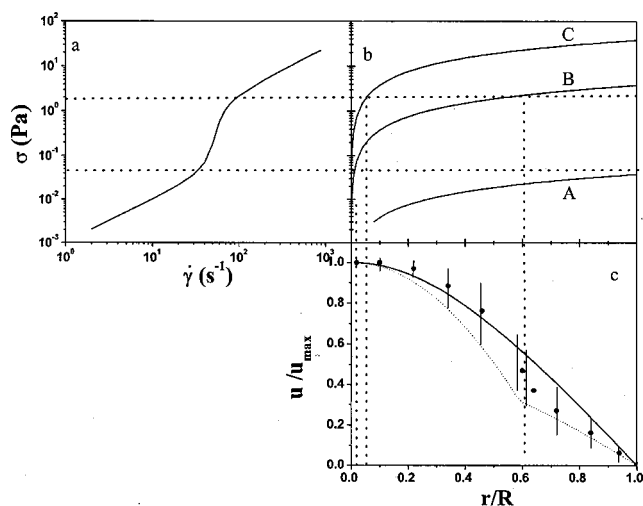

FIG. 11. Predictions of (a) shear stress vs time in steady simple shear flow, (b) shear stress as a function of the radial position, and (c) velocity profiles. Experimental data are shown by closed circles. When the stress at the wall is located in region IV, the velocity profile is composed of two parabolic regions.
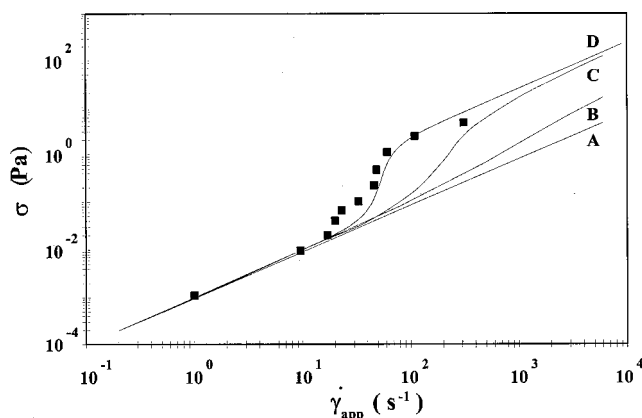
FIG. 12. Predicted shear stress at the wall vs the apparent shear rate in steady pressure flow for various L/D. Experimental data for 0.25 wt % CTAT solutions (closed squares) from cone and plate geometry are also plotted.

11(c) presents experimental point-velocity values obtained in the PIV apparatus (closed circles) for various apparent shear rates plotted with the model predictions of the velocity profile (the shear rate is 152 s^{-1}). Notice that in the region of transition corresponding to that in regime II, the error bars denote fluctuations in the measured point velocities, whereas the predictions depict the change in curvature in the transition region. In the vicinity of the wall, there is an apparent increase in viscosity and the predictions of the model match the change in curvature of the experiments.

Figure 12 reports predicted values of the wall shear stress versus the apparent shear rate ($\dot{\gamma}_{app} \equiv 4Q/\pi R^3$) for several values of L/D. For short pipe lengths, the fluid does not shear thicken because the residence time is smaller than the induction time and its behavior is Newtonian (curve A). As the residence time of the liquid in the pipe increases, a gradual manifestation of shear thickening occurs (curves B and C). In Fig. 12, simple steady shear data (closed squares) are plotted with the model predictions, and they certainly follow the curve corresponding to long enough residence times for SIS to develop (curve D). These predictions illustrate the transient development of shear thickening, in which an *induction time*, related to the residence time of the liquid in the pipe, is a necessary condition for shear thickening to develop.

V. DISCUSSION

Direct observation of shear-induced structures responsible for the shear thickening observed in dilute solutions of worm-like micelles reveals four distinct regimes of flow behavior in parallel plates: a Newtonian region at low shear rates followed by a nonhomogeneous (regime II) and homogeneous (regime III) nucleation of SIS, respectively, and an apparent second Newtonian region where strong temporal and spatial fluctuations of the viscosity smoothed by plate inertia occur at high shear rates.

In parallel plates and in Poiseuille flow, the shear thickening regime is observed as a reduction in the tangential velocity in the former and in the axial velocity of the fluid close to the pipe walls in the latter. In parallel plates, the high viscosity fluid shows a lower tangential velocity and coexists with a low-viscosity fluid with larger velocity. In fact, Figs. 4–6 reveal the coexistence of high- and low-viscosity fluids when the stress applied lies in the transition region. The difference in viscosity patterns occurs because

the time scale of the fluctuations in the viscosity differs in each regime. In regime II (Figs. 3 and 4) the time scale of the fluctuations is large and only a single thickened state is observed. In regime III (Figs. 3 and 5) the time scale of the fluctuations decreases and maxima and minima in the viscosity corresponding to low- and high-velocity regions coexisting are detected. In regime IV (Figs. 3 and 6) the time scale of viscosity fluctuations is very short and the velocity fluctuations are very large. The apparent second Newtonian region corresponds to inertia-smoothed viscosity fluctuations.

For a given applied pressure gradient within the transition region [Fig. 11(c)], regions of shear thickening behavior appear in the vicinity of the walls. The shear rate at the wall is smaller than that resulting from extrapolation of the parabolic profile of regime I to the wall. Fluctuations in pressure flow are observed in the transition region between the parabolic profiles, i.e., the region corresponding to the onset for shear thickening. PIV results show a smoothed-out region at high shear rates. The model predictions are in agreement with these observations.

In Poiseuille flow, the velocity profile gradually changes from a Newtonian parabola into that composed of the superposition of two parabolic profiles, where shear thickening occurs. The induction time for shear thickening is that defined by the onset of the second parabolic profile next to the walls, and it is shorter for increasing pressure gradients. If the residence time of the fluid in the pipe is smaller than the induction time, the behavior is Newtonian. Otherwise, shear thickening develops. This is in agreement with experimental data in simple shear reported elsewhere [Hu *et al.* (1993); Gámez-Corrales *et al.* (1999); Macías *et al.* (2001)] which show that the induction time is inversely proportional to the shear rate applied.

Our results show that both $\dot{\gamma}_c$ and σ_c shift toward higher values with an increase in concentration up to the transition to shear thinning (Fig. 7), similar to results reported elsewhere [Gámez-Corrales *et al.* (1999)]. Our model also predicts similar trends. These cause shifting of curve σ vs $\dot{\gamma}$ toward larger shear rates, so the magnitude of the increase of shear viscosity diminishes, as discussed previously.

Finally, it is necessary to remark that predictions of the fluctuating patterns of the viscosity and tangential velocity can only be realized if consideration is given to the coupling between the SIS and the flow. The presentation of parallel plates and pressure flow data was intended to show experimental evidence of the shear thickening transition in inhomogeneous flows, where the shear rate changes with the radial distance. Predictions of the model in steady state can only show average extreme values of the fluctuating patterns of velocity profiles, and this can improve understanding of the overall response of the system. The presence of the SIS was modeled here as an increase in dissipation of the system is a result of a more structured state.

ACKNOWLEDGMENTS

References

Bautista, F., J. M. de Santos, J. F. A. Soltero, J. E. Puig, and O. Manero, ''Understanding thixotropic and antithixotropic behavior of viscoelastic micellar solutions and liquid crystalline dispersions. I. The model,'' J. Non-Newtonian Fluid Mech. **80**, 93–113 (1999).

Bautista, F., J. F. A. Soltero, E. R. Macías, J. E. Puig, and O. Manero, ''Thermodynamics approach and modelling of shear banding flow of wormlike micelles,'' J. Phys. Chem. B **106**, 13018–13026 (2002).

Bautista, F., J. F. A. Soltero, J. H. Perez-Lopez, J. E. Puig, and O. Manero, ''On the shear banding flow of elongated micellar solutions,'' J. Non-Newtonian Fluid Mech. **94**, 57–66 (2000).

Berret, J. F., R. Gámez-Corrales, J. Oberdisse, L. M. Walker, and P. Lindner, ''Flow-structure relationship of shear thickening surfactant solutions,'' Europhys. Lett. **41**, 677–682 (1998).

Berret, J. F., R. Gámez-Corrales, Y. Serero, F. Molino, and P. Lindner, ''Shear-induced micellar growth in dilute surfactant solutions,'' Europhys. Lett. **54**, 605–611 (2001).

Gámez-Corrales, R., J. F. Berret, L. M. Walker, and J. Oberdisse, ''Shear-thickening dilute surfactant solutions: Equilibrium structure as studied by small-angle neutron scattering,'' Langmuir **15**, 6755–6763 (1999).

Goveas, J. L., and D. J. Pine, ''A phenomenological model for shear thickening in wormlike micelle solutions,'' Europhys. Lett. **48**, 706–712 (1999).

Gravsholt, S., ''Rheological properties on highly dilute viscoelastic aqueous detergent solutions,'' in *Proceedings of the VIII International Congress on Rheology,* edited by G. Astarita, G. Marucci, an L. Nicalais (Plenum Press, New York, 1980), pp. 629–633.

Hartmann, H., and R. Cressely, ''Shear thickening of an aqueous micellar solution of cetyltrimethylammonium bromide and sodium tosylate,'' J. Phys. II **7**, 1087–1098 (1997).

Hartmann, V., and R. Cressely, ''Ocurrence of shear thickening in aqueous micellar solutions of CTAB with some added organic counterions,'' Colloid Polym. Sci. **276**, 169–175 (1998).

Hoffmann, H., S. Hofmann, A. Rauscher, and J. Kalus, ''Shear-induced transitions in micellar solutions,'' Prog. Colloid Polym. Sci. **84**, 24–35 (1991).

Hu, Y. T., and E. F. Mattys, ''Characterization of micellar structure dynamics for a drag-reducing surfactant solution under shear: Normal stress studies and flow geometry effects,'' Rheol. Acta **34**, 450–460 (1995).

Hu, Y. T., P. Boltenhagen, and D. J. Pine, ''Shear thickening in low-concentration solutions of wormlike micelles. I. Direct visualization of transient behavior and phase transitions,'' J. Rheol. **42**, 1185–1208 (1998a).

Hu, Y. T., P. Boltenhagen, W. Mattys, and D. J. Pine, ''Shear thickening in low-concentration solutions of wormlike micelles. II. Slip, fracture, and stability of the Sehar-induced phase,'' J. Rheol. **42**, 1185–1208 (1998b).

Hu, Y. T., S. Q. Wang, and A. M. Jamieson, ''Rheological and flow birefringence studies of a shear-thickening complex fluid-*A* surfactant model system,'' J. Rheol. **37**, 531–546 (1993).

Kalus, J., H. Hoffmann, and P. Lindner, ''Small-angle neutron scattering experiments of micellar solutions under shear,'' Prog. Colloid Polym. Sci. **79**, 233–238 (1989).

Koch, S., T. Schneider, and E. Küter, ''The velocity field of dilute cationic surfactant solutions in a Couette viscometer,'' J. Non-Newtonian Fluid Mech. **78**, 47–59 (1998).

Liu, C. H., and D. J. Pine, ''Shear induced gelation and fracture in micellar solutions,'' Phys. Rev. Lett. **77**, 2121–2124 (1996).

Macías, E. R., A. González, O. Manero, R. González Núñez, J. F. A. Soltero, and P. Atanné, ''Flow regimes of dilute surfactant solutions,'' J. Non-Newtonian Fluid Mech. **101**, 149–171 (2001).

Manero, O., F. Bautista, J. F. A. Soltero, and J. E. Puig, ''Dynamics of worm-like micelles: The Cox–Merz rule,'' J. Non-Newtonian Fluid Mech. **106**, 1–15 (2002).

Olmsted, P. D., and C.-Y. D. Lu, ''Coexistence and phase separation in sheared complex fluids,'' Phys. Rev. E **56**, 55–58 (1997).

Porte, G., J. F. Berret, and J. L. Harden, ''Inhomogeneous flows of complex fluids: Mechanical instability versus nonequilibrium phase transition,'' J. Phys. II **7**, 459–472 (1997).

Prötzl, B., and J. Springer, ''Light scattering experiments on shear induced structures of micellar solutions,'' J. Colloid Interface Sci. **190**, 327–333 (1997).

Rehage, H., and H. Hoffmann, ''Shear induced phase transitions in highly dilute aqueous detergent solutions,'' Rheol. Acta **21**, 561–563 (1982).

Rehage, H., I. Wunderlich, and H. Hoffmann, ''Shear induced phase transactions in dilute aqueous surfactant solutions,'' Prog. Colloid Polym. Sci. **72**, 51–59 (1986).

Soltero, J. F. A., J. E. Puig, and O. Manero, ''Rheology of the cetyltrimethylammonium tosilate-water system. 2. Linear viscoelastic regime,'' Langmuir **12**, 2654–2662 (1996).

Soltero, J. F. A., F. Bautista, J. E. Puig, and O. Manero, ''Rheology of cetyltrimethyl ammonium *p*-toluenesulfonate-water system. 3. Nonlinear viscoelasticity,'' Langmuir **15**, 1604–1612 (1999).

Wunderlich, A. M., and P. O. Brunn, ''The complex rheological behavior of an aqueous cationic surfactant solution investigated in a Couette-type viscometer,'' Colloid Polym. Sci. **267**, 627–636 (1989).

Wunderlich, I., H. Hoffmann, and H. Rehage, ''Flow birefringence and rheological measurements on shear induced micellar structures,'' Rheol. Acta **26**, 532–542 (1987).